ELSEVIER

Chemical Engineering Journal 91 (2003) 3–22

Chemical Engineering Journal

www.elsevier.com/locate/cej

Local hydrodynamic properties of gas phase in an internal-loop airlift reactor

Cheng-Shing Lo, Shyh-Jye Hwang*

Department of Chemical Engineering, National Tsing Hua University, Hsinchu, Taiwan, ROC

Received 8 September 2001; accepted 26 March 2002

Abstract

The local hydrodynamic properties of the gas phase in an internal-loop airlift reactor were investigated in this study. The hydrodynamic properties including gas holdup, bubble velocity and bubble chord length were measured by dual electrical resistivity probes. The chord length distribution was then transformed to the bubble size distribution by modeling the bubbles as ellipsoids. It was found that the gas holdup increased with decreasing bubble velocity. In addition, most bubbles tended to rise along the riser central axis. Thus, the gas holdup in the axis was higher. The bubble size, bubble velocity and gas holdup were relatively constant in the axial direction of the riser except in the zones near the gas sparger and the gas–liquid separator. The bubble velocity became slower when the bubbles approached the gas–liquid separator. Moreover, the bubble size and bubble velocity for the three-phase system were relatively insensitive to the radial direction compared to those for the two-phase system. It was also found in this study that the bubble rise velocity and bubble size for the three-phase system were lower than that for the two-phase system. However, the gas holdup for the three-phase system were higher than that for the two-phase system due to bubble breakage caused by the solid particles.

Keywords: Internal-loop airlift reactor; Local hydrodynamic properties; Gas phase

1. Introduction

Airlift reactors are widely employed in many biochemical processes such as aerobic fermentation and wastewater treatment. Some of the important hydrodynamic parameters of the airlift reactors are gas holdup, bubble rise velocity, bubble size and specific interfacial area [1]. Because of difficulties associated with direct measurements of the local gas phase hydrodynamics in the airlift reactors, experimental results are limited in the literature.

Matsuura and Fan [2] measured the distributions of the bubble properties including bubble size and bubble velocity at the center of a gas–liquid–solid fluidized bed. The distributions of the bubble properties were evaluated for three flow regimes: dispersed bubble flow regime, coalesced bubble flow regime, and slug flow regime. Fan et al. [3] measured the bubble size distribution and gas holdup at the center of a gas–liquid–solid annular fluidized bed, and pointed out that the addition of a concentrically located inner column promoted bubble coalescence. Also, the bubble sizes were smaller for the fluidization of 3 mm glass beads than those of 1 mm glass beads. Yasunishi et al. [4] measured the bubble properties such as gas holdup, bubble frequency, bubble length and bubble velocity at the center of a slurry bubble column. Bentifraouine et al. [5] measured the local gas phase characteristics in an external-loop airlift reactor filled with Newtonian or non-Newtonian liquids. They pointed out that the bubble coalescence and the break-up phenomena were different in different liquids and levels in the riser. Utiger et al. [6] measured the local flow characteristics in the riser of a two-phase external loop airlift reactor. They found that as the gas flow rate increased, the bubble diameter increased and the radial gas holdup profile changed from relatively flat to parabolic while the shape of the radial liquid velocity profile remained constant.

Up to now, the study of the local gas phase hydrodynamics in a internal-loop airlift reactor has been rare. For example, Miyahara et al. [7] measured the bubble size distribution in a bubble column with a draught tube and a sieve plate was used as the gas distributor. Bubbles formed from the sieve plate were photographed with a camera and the measured point was located at 30 cm above the sieve plate. Therefore, the principal objective of this study was to investigate extensively the local gas phase hydrodynamic properties in an internal-loop airlift reactor. The local gas phase hydrodynamic properties including gas holdup, bubble velocity and bubble size were measured by using the

* Corresponding author. Tel.: +886-35723221; fax: +886-35715408.
E-mail address: sjhwang@che.nthu.edu.tw (S.-J. Hwang).

1385-8947/02/$ – see front matter
PII: S1385-8947(02)00042-6

Nomenclature

A_{ri}	area of region i (m^2)
d_b	bubble size (m)
$d_{bd(j)}$	diameter of bubbles with series number j in the downcomer (m)
d_{bmd}	local mean bubble diameter at a certain position of the downcomer (m)
d_{bmrc}	cross-sectionally averaged bubble diameter at a certain height of the riser (m)
d_{bmri}	local mean bubble diameter in region i at a certain position of the riser (m)
$d_{bri(j)}$	diameter of bubbles with series number j in region i (m)
i	region i of the riser (–)
j	serial number of bubble sample (–)
k_{mri}	local bubble number frequency per unit area in region i ($1/s\,m^2$)
L_p	vertical distance between the two tips of the probe (m)
n	number of bubble samples (–)
$P(d_{bd(j)})$	probability of the bubble with diameter $d_{bd(j)}$ (m)
$P(d_{bri(j)})$	probability of the bubble with diameter $d_{bri(j)}$ (m)
$P(u_{bd(j)})$	probability of the bubble velocity between $u_{bd(j)} - 1/2\Delta u_{bd}$ and $u_{bd(j+1)} + 1/2\Delta u_{bd}$ (–)
$P(u_{bri(j)})$	probability of the bubble velocity between $u_{bri(j)} - 1/2\Delta u_{bri}$ and $u_{bri(j+1)} + 1/2\Delta u_{bri}$ (–)
$P_p(R)$	radius distribution of bubbles touching the probe (1/m)
$P_c(y)$	chord length distribution (1/m)
r	radius (m)
R	bubble radius with ellipsoidal shape model (m)
t	real time or dwell time (s)
T	measuring period (s)
u_b	bubble velocity (m/s)
$u_{bd(j)}$	downward velocity of bubbles with serial number j in the downcomer (m/s)
$u_{bd(max)}$	maximum bubble velocity in the downcomer (m/s)
u_{bj}	velocity of bubble with serial number j (m/s)
u_{bm}	mean bubble velocity (m/s)
u_{bmd}	mean bubble downward velocity in the downcomer at a certain height (m/s)
u_{bmrc}	cross-sectionally averaged bubble velocity at a certain height of the riser (m/s)
u_{bmri}	local mean bubble rise velocity in region i at a certain position of the riser (m/s)
$u_{bri(j)}$	rise velocity of bubbles with serial number j in region i (m/s)
$u_{bri(max)}$	maximum bubble velocity in region i of the riser (m/s)
V_s	superficial gas velocity (m/s)
y	chord length (m)

Greek letters

α	shape factor (–)
ε_{gd}	local gas holdup at a certain position of the downcomer (–)
ε_{gmrc}	cross-sectionally averaged gas holdup at a certain height of the riser (–)
ε_{gr}	local gas holdup at a certain position in the riser (–)
ε_{gri}	local gas holdup at a certain position of region i in the riser (–)
μ	parameter of the Rayleigh function (–)
τ	dwell time (s)
$\Delta\tau$	average residence time of a bubble travelling between the two tips of the probe (s)
$\tau_{d(j)}$	dwell time of the bubble with serial number j in the downcomer (s)
$\tau_{ri(j)}$	dwell time of the bubble with serial number j in region i (s)
τ_1	the dwell time during passing through the tip 1 of a bubble (s)
τ_2	the dwell time during passing through the tip 2 of a bubble (s)

dual electrical resistivity probe method [2,3,8,9]. The results were then analyzed in detail.

2. Experimental

2.1. Apparatus

The diagram of the experimental setup is shown in Fig. 1. This reactor consisted of a cylindrical vessel, 18 cm in inside diameter and 230 cm in height, and a concentric draft tube 12 cm in inside diameter and 170 cm in height. The draft tube was located 10 cm above the base of the reactor. The unaerated liquid height was kept at 200 cm and the top clearance (the distance between the liquid surface and the upper end of the draft tube) was 20 cm. The gas was dispersed by a ring sparger located at the bottom of the draft tube with a ring diameter of 10 cm. There were 1 mm holes on the sparger with 1 cm between two holes. The superficial gas velocity was regulated by flowmeters. Three superficial gas velocities (0.71, 2.13 and 3.55 cm/s) were used. Both gas–liquid and gas–liquid–solid systems were studied. For the three-phase system, the solid holdup was kept at 5% by volume. Water was used as the liquid phase, air as the gas phase and polystyrene particles as the solid phase. The density and equivalent diameter of the polystyrene particles were 1050 kg/m^3 and 3 mm, respectively.

2.2. Probe system and data acquisition

Fig. 2 is the sketch of the probe system. The dual electrical resistivity probe consisted of two enamel-insulated wires 0.15 mm in diameter. The tips of the wires were exposed and the vertical distance between the two wires was 0.3 mm. The wires were coated by epoxy resin and supported by a stainless tube. The hydrodynamic properties including gas holdup, bubble velocity and bubble chord length were measured at six axial positions of the riser and downcomer of

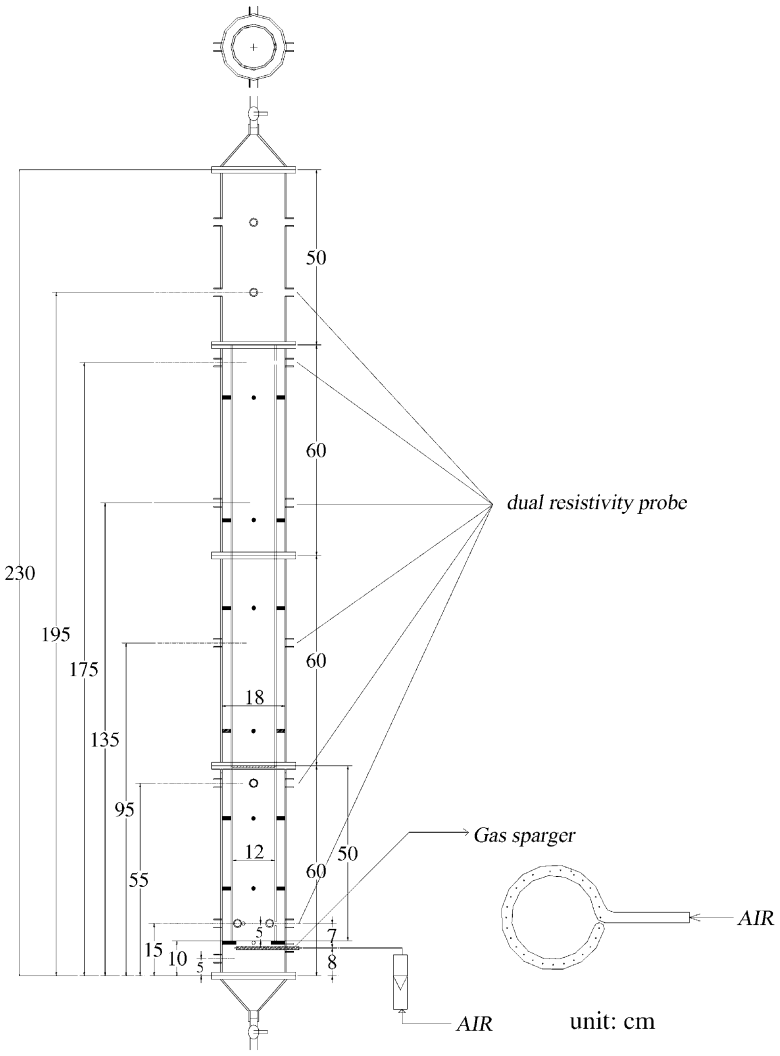

Fig. 1. Schematic diagram of the airlift reactor and gas sparger.

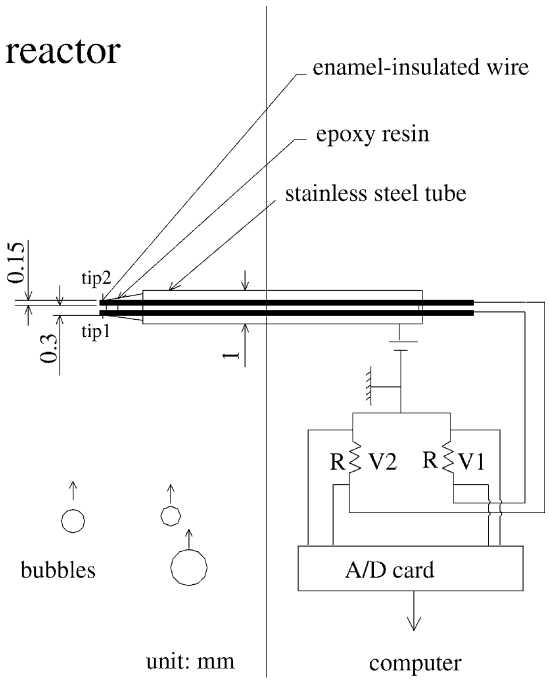

Fig. 2. Sketch of the probe system and signal flow.

the reactor, i.e., 15, 55, 95, 135, 175 and 195 cm from the base of the reactor. In addition, measurements were taken at three radial positions in the riser, i.e., 0, 3 and 5 cm from the axis of the draft tube, and one radial position in the downcomer, i.e., 7.5 cm from the axis of the draft tube. The data obtained by the probe were stored in a computer for further processing.

2.3. Signal processing

The signals obtained by the probe were used to obtain some parameters that characterize the local hydrodynamic behavior of the gas phase, e.g., gas holdup, bubble velocity, chord length distribution of the bubbles [4,6,10–13]. The acquisition frequency was 100 kHz, high enough to measure the properties of very fast bubbles passing through the small distance between the two tips of the probe. Thus very small bubbles could also be detected. Typical signals when a bubble passed through the probe tips are shown in Fig. 3. It is noted that the dwell time τ_1 and τ_2 in Fig. 3 are the time that a bubble spends at tips 1 and 2, respectively. The analog signals from the probe were amplified to high-level signals, i.e., 5 V for liquid contacting probe tip. The threshold signal intensity was set at 80% of the high level signal intensity, i.e., 4 V [14]. Typical reformed signals are shown in Fig. 4. The local gas holdup could then be determined as the ratio of the sum of the dwell time for the bubbles to the measuring period. The bubble rise velocity, u_b, and chord length, y, were calculated by the following equations [2,3,9]:

$$u_b = \frac{L_p}{\Delta\tau} \tag{1}$$

$$y = \frac{\tau_1 + \tau_2}{2} u_b \tag{2}$$

where L_p is the vertical distance between the two tips of the probe and $\Delta\tau$ the average residence time of a bubble travelling between the two tips of the probe. $\Delta\tau$ could be expressed by [2]:

$$\Delta\tau = (t_2 - t_1) + \tfrac{1}{2}(\tau_2 - \tau_1) = \Delta t + \tfrac{1}{2}(\tau_2 - \tau_1) \tag{3}$$

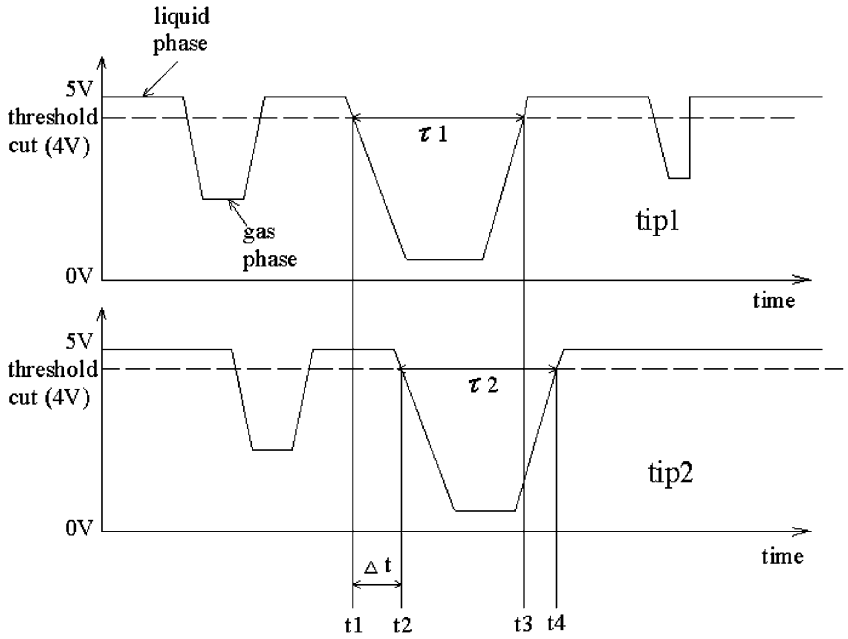

Fig. 3. Typical signals when a bubble was passing through the probe tips.

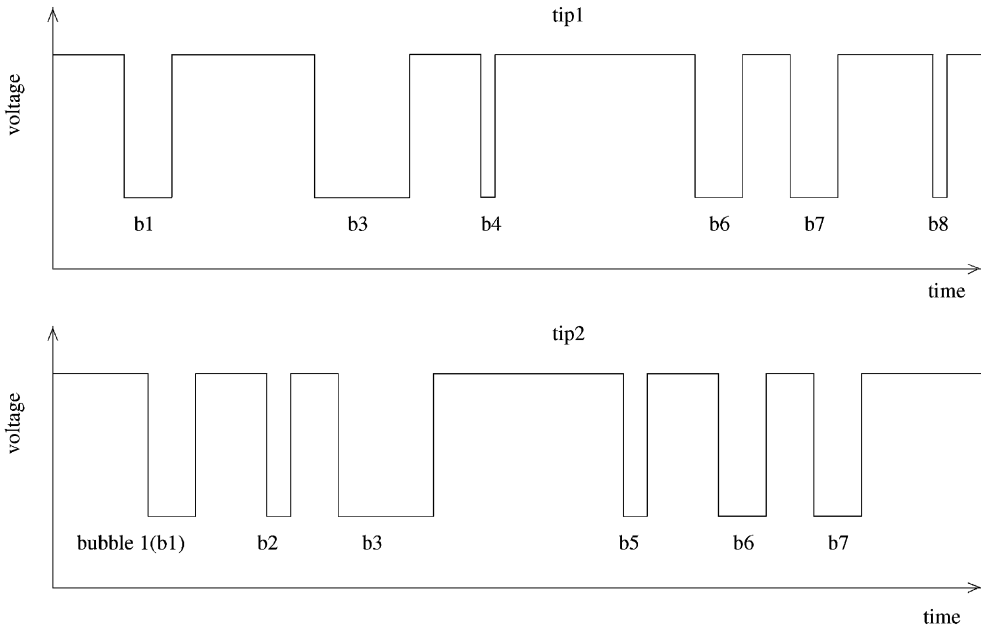

Fig. 4. Reformed signals as a function of time.

where t_1 and t_2 represent the real time when a bubble touch tips 1 and 2, and τ_1 and τ_2 are the dwell time that a bubble spends at tips 1 and 2.

The mean bubble velocity was obtained by [15]:

$$u_{\mathrm{bm}} = \frac{1}{n}\sum_{j=1}^{n} u_{\mathrm{b}j} \tag{4}$$

It should be noted that it was necessary to 'couple' the signals from the two tips of the probe for each bubble detected in order to find the bubble velocity and bubble chord length. For example, only bubbles 1, 3, 6 and 7 in Fig. 4 were taken into account to calculate the chord length and bubble velocity because they were detected by both tips [10]. Moreover, signal pairs were accepted if they satisfied the following conditions [2]:

1. $t_1 < t_2$.
2. $t_1 + \tau_1 < t_2 + \tau_2$.
3. $0.9 < \tau_1/0.5(\tau_1 + \tau_2) < 1.1$.

Signal pairs that did not satisfy the above conditions were deleted automatically when the experimental data were processed by our computer program.

In this study, the method of Liu and Clark [16] was employed to transform the chord length distribution into the equivalent bubble diameter distribution. As shown in Fig. 5, bubbles were considered to be ellipsoidal, and the shape factor α was assumed to be 0.8 [17]. Note that the equivalent bubble diameter is the volume-equivalent spherical bubble diameter [18], and is equal to $2\sqrt[3]{\alpha}R$. This diameter was designated as the bubble size in this study.

The least squares best fit method was used to fit the probability histogram of the experimentally measured chord length distribution with Rayleigh probability function [16]:

$$P_{\mathrm{c}}(y) = \frac{y}{\mu^2}\exp\left[\frac{-y^2}{2\mu^2}\right] \tag{5}$$

The value of μ found in Eq. (5) was used to obtain $P_{\mathrm{p}}(R)$:

$$P_{\mathrm{p}}(R) = \frac{R^3}{2(\mu/2\alpha)^4}\exp\left[\frac{-R^2}{2(\mu/2\alpha)^2}\right] \tag{6}$$

where $P_{\mathrm{p}}(R)$ is the radius distribution of the bubbles touching the probe.

$P_{\mathrm{p}}(R)$ could be easily transformed into bubble size distribution, $P(d_{\mathrm{br}i})$ and a schematic diagram of a typical bubble size distribution is shown in Fig. 6.

2.4. The local mean and cross-sectionally averaged gas phase hydrodynamic properties

The cross-section of the riser was divided into three regions as shown in Fig. 7. The area of regions 1, 2 and 3,

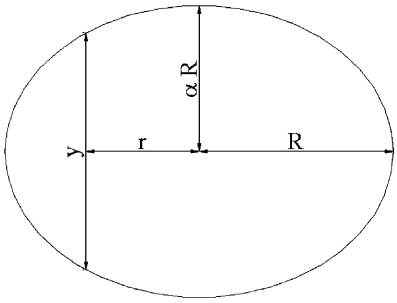

Fig. 5. Ellipsoidal shape bubble model [16].

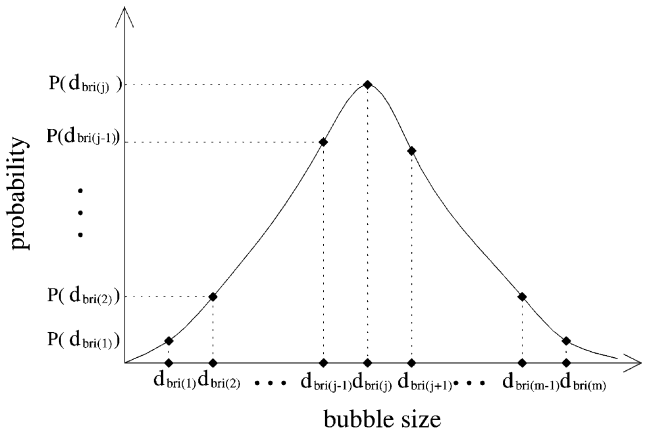

Fig. 6. A schematic diagram of a typical bubble size distribution.

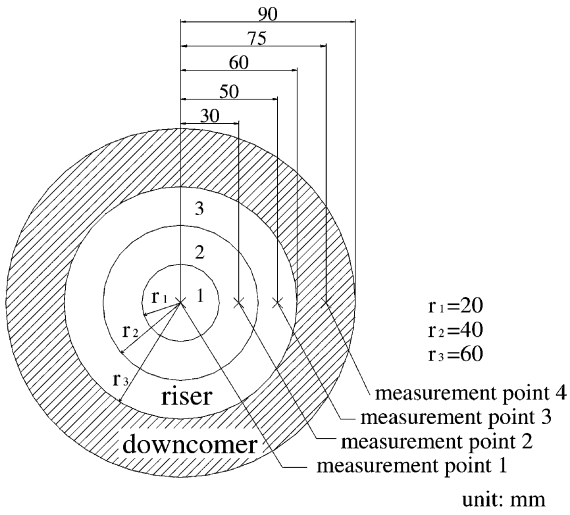

Fig. 7. Various regions of the riser and downcomer.

i.e., A_{r1}, A_{r2} and A_{r3}, are πr_1^2, $\pi(r_2^2 - r_1^2)$ and $\pi(r_3^2 - r_2^2)$, respectively. Local mean bubble diameter in region i at a certain position of the riser is [7]:

$$d_{bmri} = \sum_{j=1}^{m} d_{bri(j)} \times P(d_{bri(j)}) \quad (7)$$

where $d_{bri(j)}$ is the diameter of the bubbles with serial number j in region i, and $P(d_{bri(j)})$ the probability of the bubbles with diameter $d_{bri(j)}$ shown in Fig. 6.

Consider a set of data consisting of n observations of the bubble velocity u_{bri} in region i, and as shown in Fig. 8, the data were divided into m equal partitions such that

$$u_{bri(j)} = u_{bri(max)} - (j + \tfrac{1}{2})\Delta u_{bri}, \quad 0 \leqq j \leqq m-1 \quad (8)$$

where $\Delta u_{bri} = u_{bri(max)}/m$ and $u_{bri(max)}$ is the maximum bubble velocity of the measurements.

Local mean bubble rise velocity in region i at a certain position of the riser could then be calculated [15]:

$$u_{bmri} = \sum_{j=0}^{m-1} u_{bri(j)} \times P(u_{bri(j)}) \quad (9)$$

where $u_{bri(j)}$ is the jth bubble velocity, and $P(u_{bri(j)})$ the probability of the bubble velocity between $u_{bri(j)} - \frac{1}{2}\Delta u_{bri}$ and $u_{bri(j)} + \frac{1}{2}\Delta u_{bri}$ shown in Fig. 8.

Local gas hold up in region i at a certain position of the riser is the ratio of the sum of the dwell time for the bubbles to the measuring period [4]:

$$\varepsilon_{gri} = \frac{\sum_{j=1}^{n} \tau_{ri(j)}}{T} \quad (10)$$

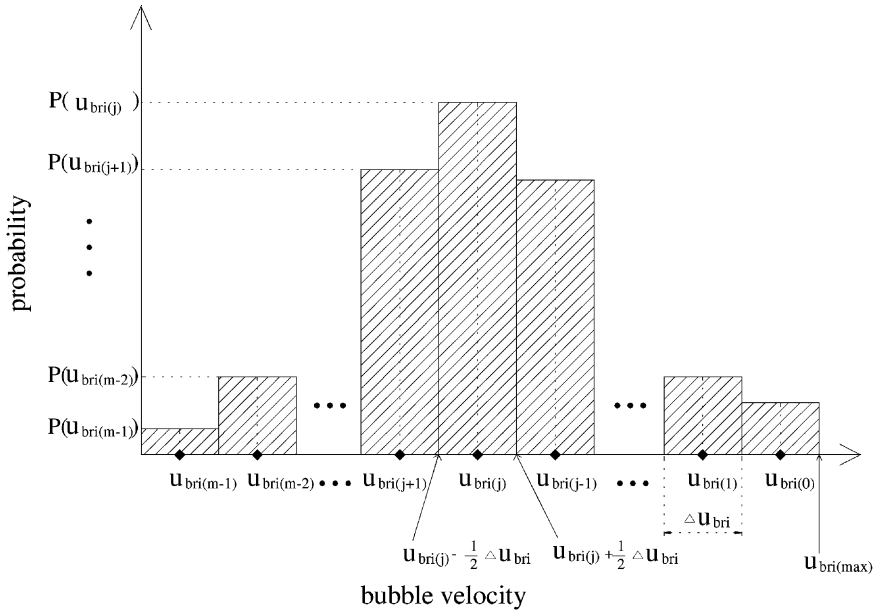

Fig. 8. A typical bubble velocity distribution.

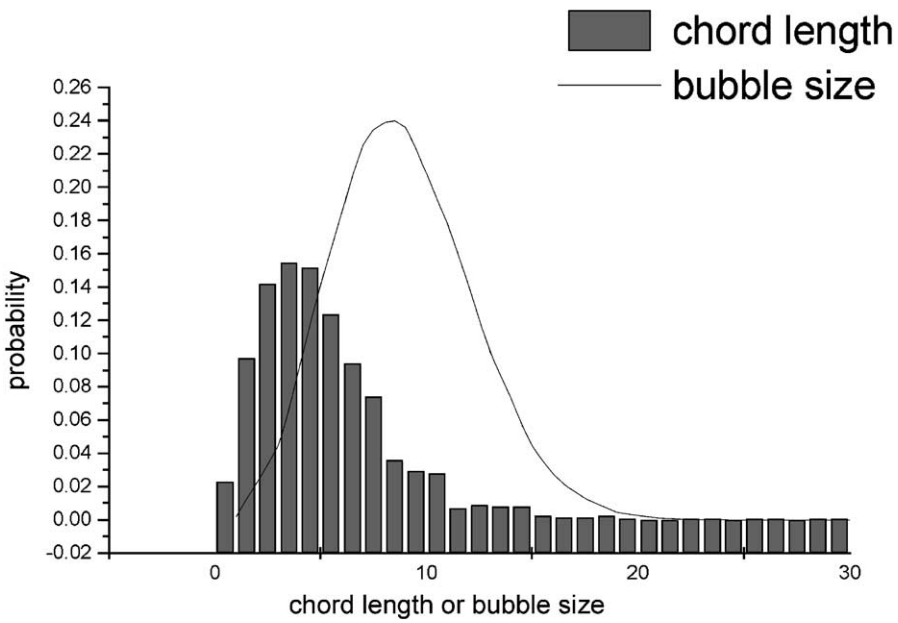

Fig. 9. A typical probability histogram of the chord length and the corresponding bubble size distribution.

where $\tau_{ri(j)}$ is the dwell time of the bubble with serial number j passing through one tip of probe in region i, and T the measuring period.

Similarly, the local mean bubble diameter, bubble downward velocity and gas holdup at a certain position in the downcomer are:

$$d_{\mathrm{bmd}} = \sum_{j=1}^{m} d_{\mathrm{bd}(j)} \times P(d_{\mathrm{bd}(j)}) \tag{11}$$

$$u_{\mathrm{bmd}} = \sum_{j=0}^{m-1} u_{\mathrm{bd}(j)} \times P(u_{\mathrm{bd}(j)}) \tag{12}$$

$$\varepsilon_{\mathrm{gd}} = \frac{\sum_{j=1}^{n} \tau_{\mathrm{d}(j)}}{T} \tag{13}$$

where $d_{\mathrm{bd}(j)}$ is the diameter of the bubbles with serial number j in the downcomer, $P(d_{\mathrm{bd}(j)})$ the probability of the

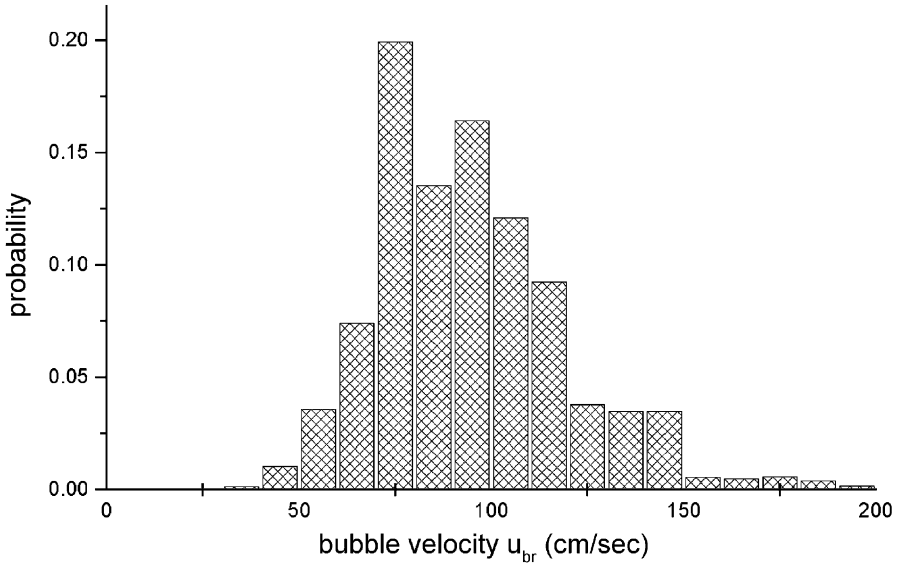

Fig. 10. A typical probability histogram of bubble rise velocity.

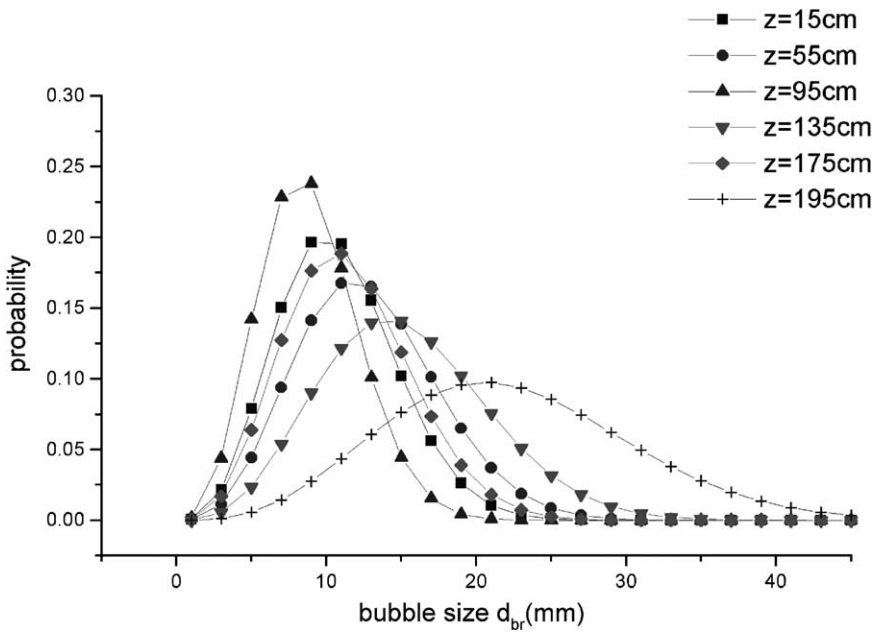

Fig. 11. Bubble size distributions in two-phase system along the central axis of the riser ($V_s = 2.13$ cm/s).

bubbles with diameter $d_{bd(j)}$, $u_{bd(j)}$ the jth bubble velocity, $P(u_{bd(j)})$ the probability of the bubble velocity between $u_{bd(j)} - \frac{1}{2}\Delta u_{bd}$ and $u_{bd(j)} + \frac{1}{2}\Delta u_{bd}$, $\Delta u_{bd} = u_{bd(max)}/m$, $u_{bd(max)}$ the maximum bubble velocity of the measurements, and $\tau_{d(j)}$ the dwell time of the bubble with serial number j in the downcomer.

Note that $u_{bd(j)}$ is obtained by

$$u_{bd(j)} = u_{bd(max)} - (j + \tfrac{1}{2})\Delta u_{bd}, \quad 0 \leqq j \leqq m - 1 \tag{14}$$

The cross-sectionally averaged gas holdup and bubble velocity at a certain height of the riser are then, respectively, expressed as [4,19]

$$\varepsilon_{gmrc} = \frac{\varepsilon_{gr1}A_{r1} + \varepsilon_{gr2}A_{r2} + \varepsilon_{gr3}A_{r3}}{A_{r1} + A_{r2} + A_{r3}} \tag{15}$$

$$u_{bmrc} = \frac{u_{bmr1}\varepsilon_{gr1}A_{r1} + u_{bmr2}\varepsilon_{gr2}A_{r2} + u_{bmr3}\varepsilon_{gr3}A_{r3}}{\varepsilon_{gr1}A_{r1} + \varepsilon_{gr2}A_{r2} + \varepsilon_{gr3}A_{r3}} \tag{16}$$

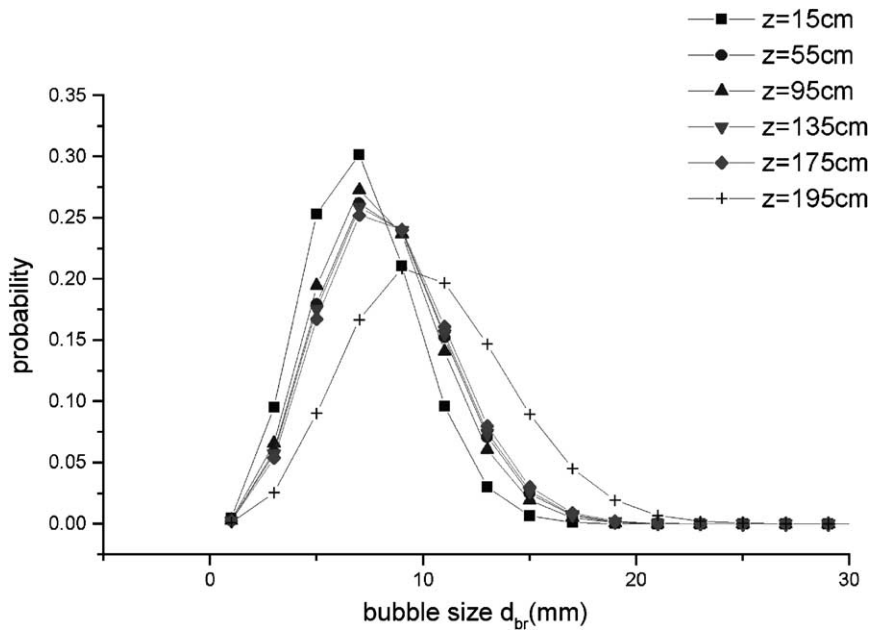

Fig. 12. Bubble size distributions in three-phase system along the central axis of the riser ($V_s = 2.13$ cm/s).

Similarly, the cross-sectionally averaged bubble diameter is:

$$d_{\mathrm{bmrc}} = \frac{d_{\mathrm{bmr1}}k_{\mathrm{mr1}}A_{\mathrm{r1}} + d_{\mathrm{bmr2}}k_{\mathrm{mr2}}A_{\mathrm{r2}} + d_{\mathrm{bmr3}}k_{\mathrm{mr3}}A_{\mathrm{r3}}}{k_{\mathrm{mr1}}A_{\mathrm{r1}} + k_{\mathrm{mr2}}A_{\mathrm{r2}} + k_{\mathrm{mr3}}A_{\mathrm{r3}}} \tag{17}$$

where $k_{\mathrm{mr}i}$ ($i = 1$, 2 or 3) is bubble number frequency per unit cross-sectional area in region i at a certain position of the riser, and is defined as

$$k_{\mathrm{mr}i} = \frac{6u_{\mathrm{bmr}i}\varepsilon_{\mathrm{gr}i}}{\pi d_{\mathrm{bmr}i}^3} \tag{18}$$

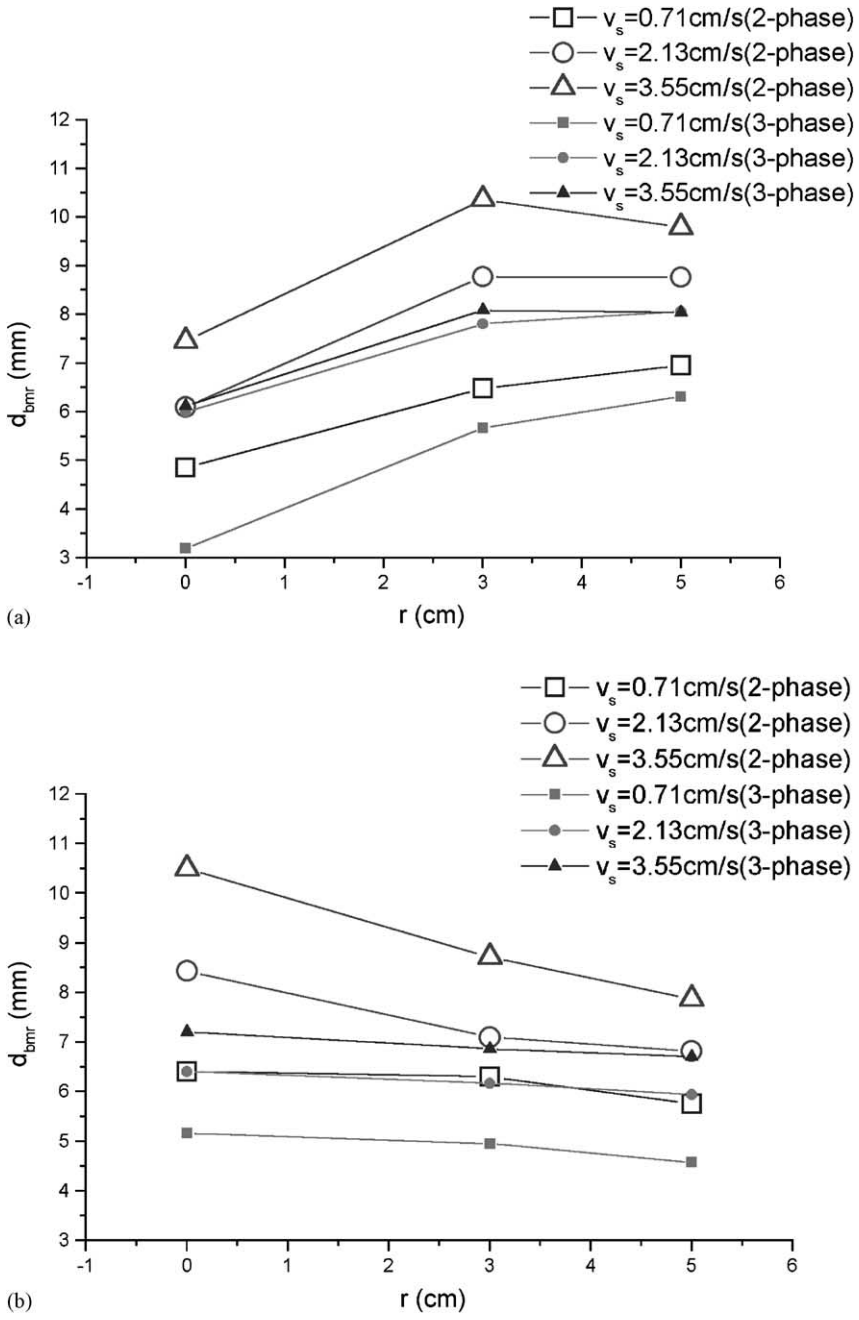

Fig. 13. (a) Mean bubble size vs. radial position at $z = 15$ cm under various superficial gas velocities. (b) Mean bubble size vs. radial position at $z = 55$ cm under various superficial gas velocities. (c) Mean bubble size vs. radial position at $z = 95$ cm under various superficial gas velocities. (d) Mean bubble size vs. radial position at $z = 135$ cm under various superficial gas velocities. (e) Mean bubble size vs. radial position at $z = 175$ cm under various superficial gas velocities. (f) Mean bubble size vs. radial position at $z = 195$ cm under various superficial gas velocities. (g) Cross-sectionally averaged bubble size in the riser vs. axial position under various superficial gas velocities. (h) Mean bubble size in the downcomer vs. axial position under various superficial gas velocities.

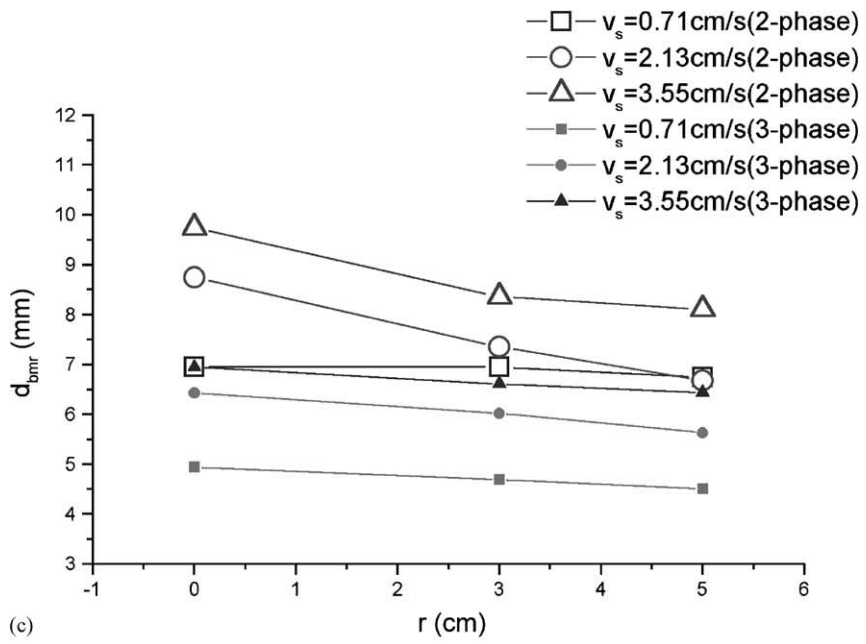

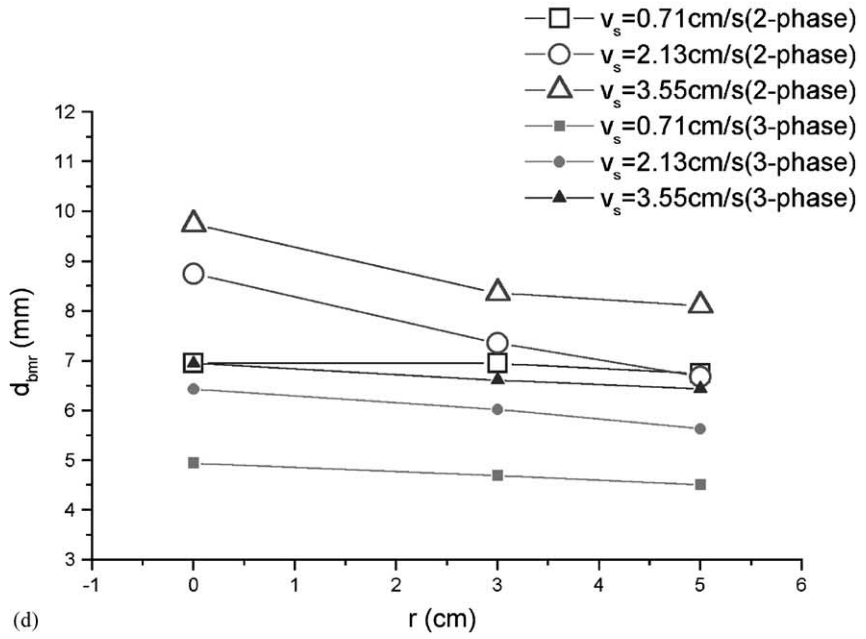

Fig. 13. (*Continued*).

3. Results and discussion

Fig. 9 is a typical probability histogram of the chord length and the bubble size distribution obtained from the chord length probability by Eqs. (5) and (6) for the two-phase system. The superficial gas velocity V_S was 2.13 cm/s and the measurement point was at the center of the riser. As expected, the bubble size distribution curve was located at the right-hand side of the chord length histogram. Fig. 10 is a typical probability histogram of the bubble velocity for the two-phase system under the same operating condition. In this case, the mean bubble velocity was around 1 m/s. Figs. 11 and 12 show the bubble size distributions for the two-phase and three-phase systems along the central axis of the riser with a superficial gas velocity of 2.13 cm/s. It is seen in Figs. 11 and 12 that the bubble size distribution curve was broader and the mean bubble size was larger at a higher axial position. In addition, the mean bubble size for the three-phase system was smaller than that for the two-phase system. In the following discussion, only the mean values of the bubble size and bubble velocity were used.

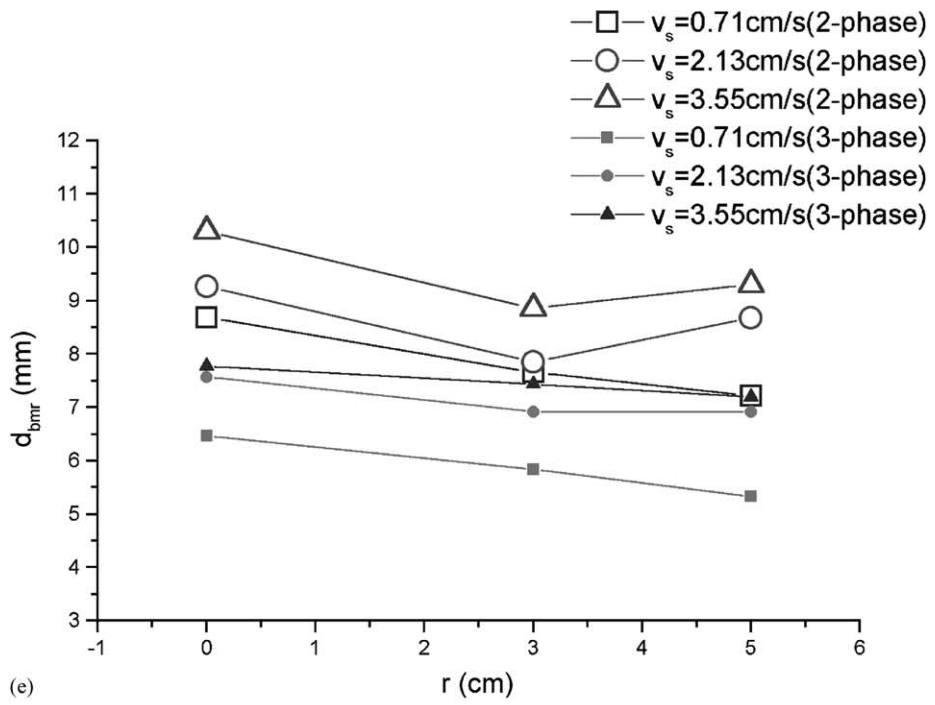

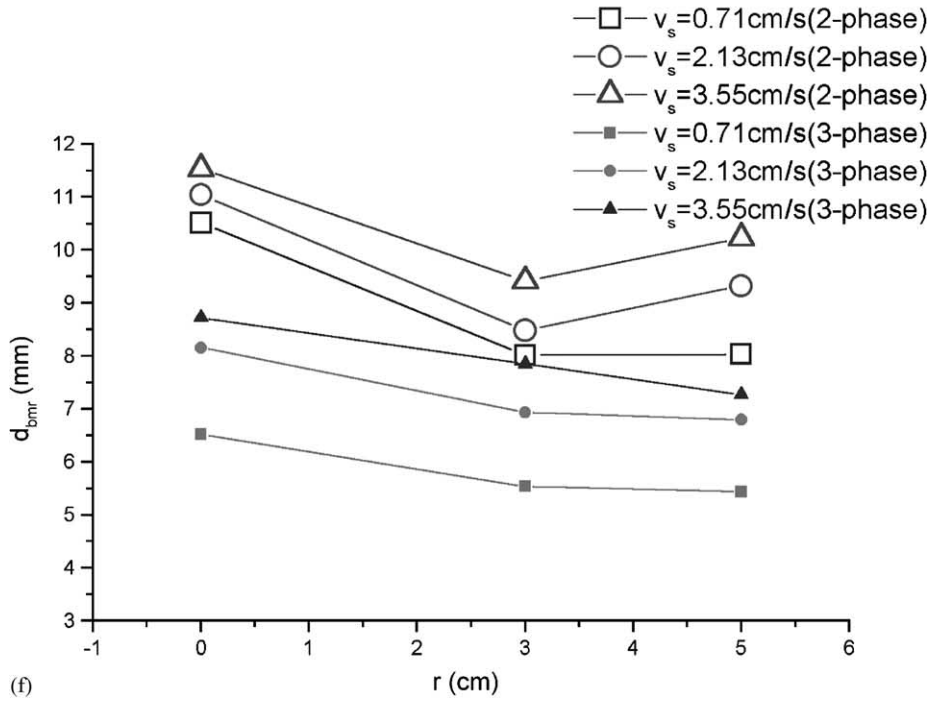

Fig. 13. (*Continued*).

3.1. Mean bubble size

Fig. 13a–f shows the radial profile of the mean bubble size in the riser for the two-phase and three-phase systems as a function of the radial position under various superficial gas velocities and axial heights. As shown in these figures, the mean bubble size in the riser was smaller than 11 mm. In addition, the mean bubble size for the three-phase system was always smaller than that for the two-phase system. This was similar to that observed by Chen and Fan in an air–water–glass bead fluidized bed [18], and was due to bubble breakage caused by particle penetration of the

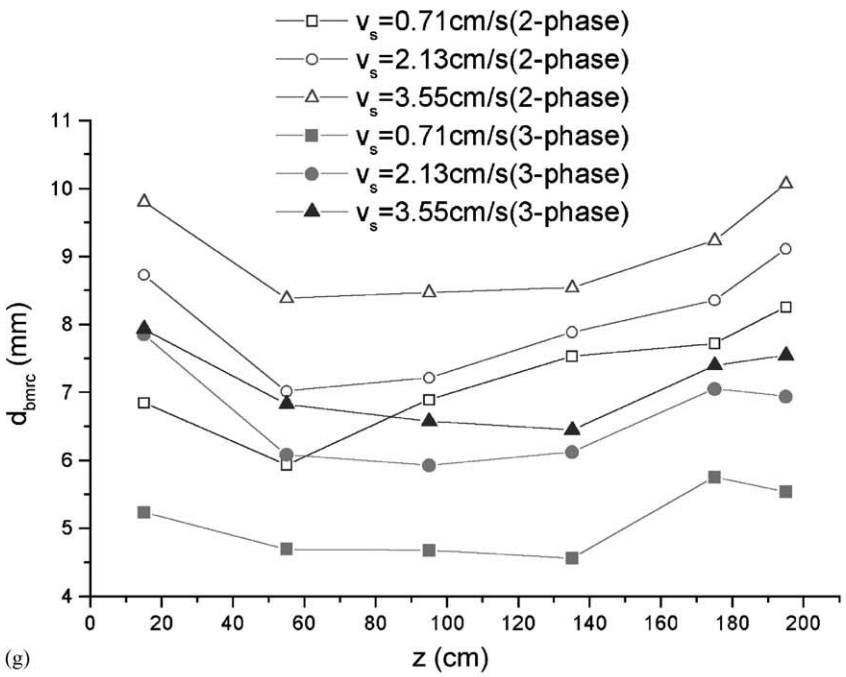

(g)

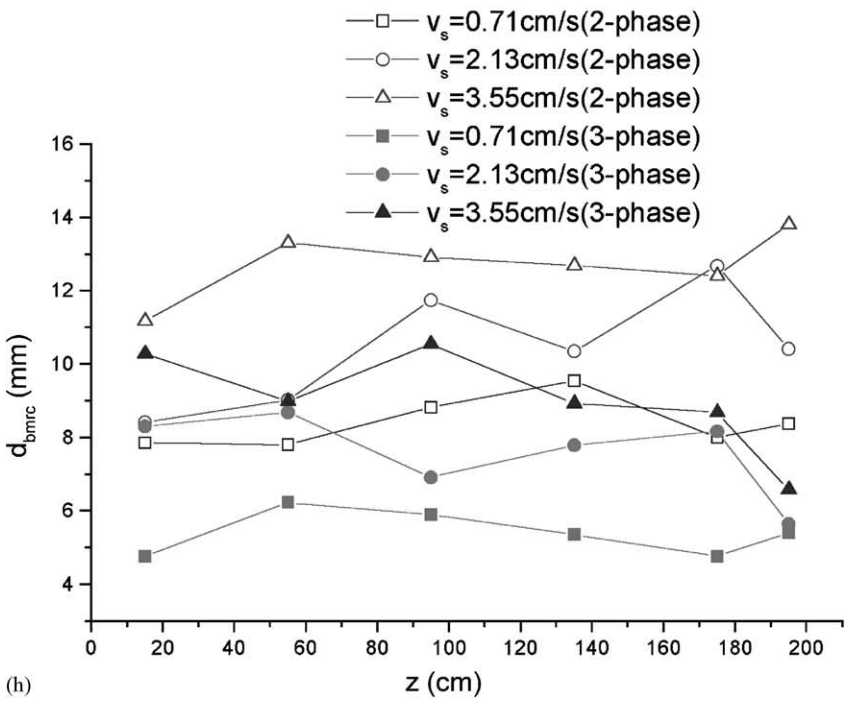

(h)

Fig. 13. (*Continued*).

bubbles. Moreover, the radial profiles of the mean bubble size for the three-phase system were flatter than those for the two-phase system. This might also be due to bubble breakage by the particles. Furthermore, the mean bubble size increased with increasing gas velocity. This was similar to that obtained by Okada et al. [20] and Wolff et al. [21] in external-loop airlift reactors.

The results presented in Fig. 13a–f also indicated that larger bubbles tended to move to the central axis as they rose upward along the riser, and the mean bubble size decreased with increasing radial position. However, the mean bubble size close to the wall of the riser becomes larger near the top of the riser ($z = 175$ cm) and in the gas–liquid separator section ($z = 195$ cm). Tan et al. [22] noted that there

existed regions of upflow and downflow of the liquid in the gas–liquid separator section above the riser. The liquid upflow occurred in the central region and the downflow occurred in the outer region near the wall of the column. As a result, many bubbles aggregated in the outer region, which enhanced bubble coalescence. Thus, the mean bubble size was larger in this region. No such phenomenon was observed in the three-phase system due to the presence of the solid particles, which impeded bubble coalescence.

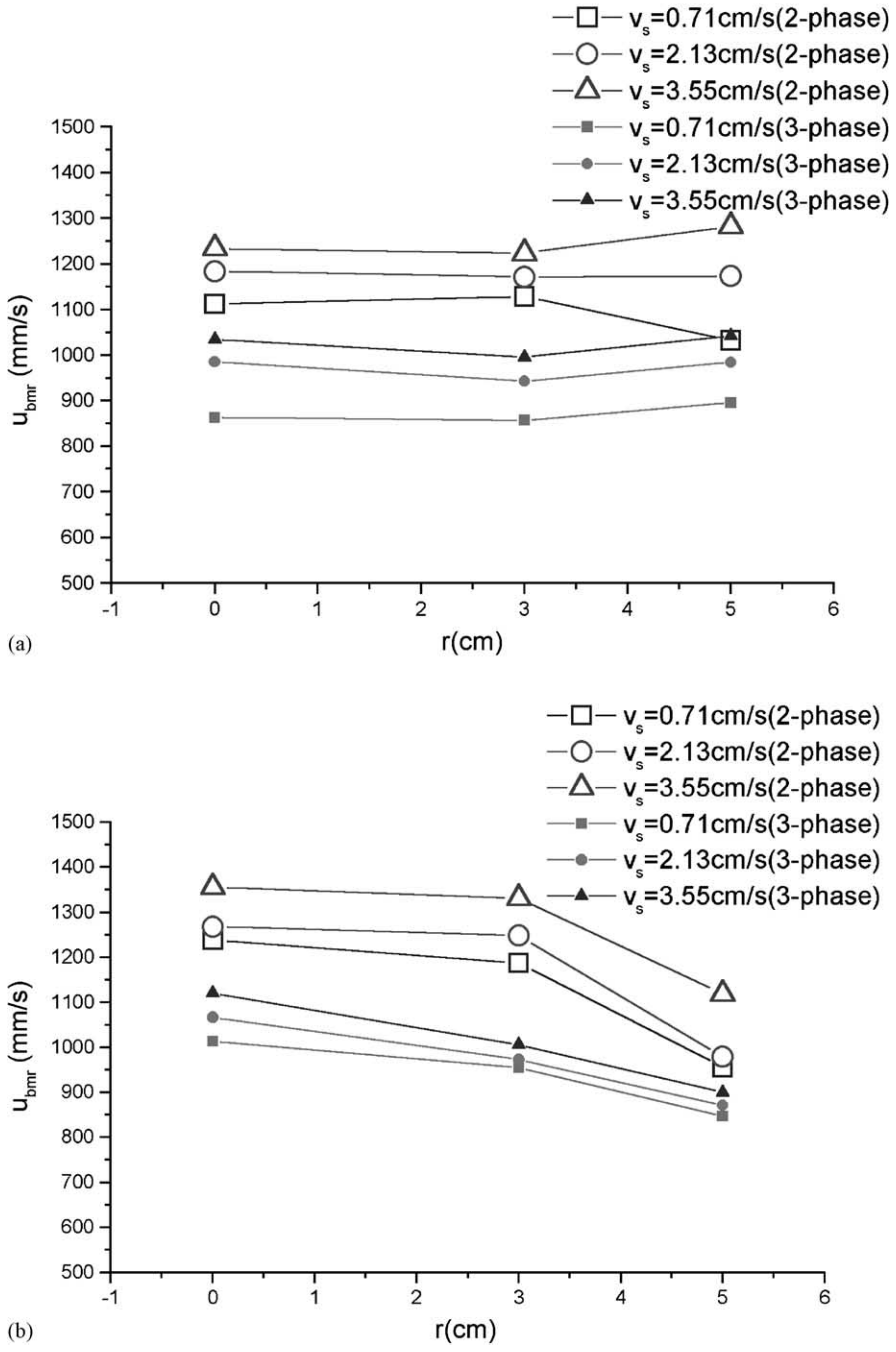

Fig. 14. (a) Mean bubble velocity vs. radial position at $z = 15$ cm under various superficial gas velocities. (b) Mean bubble velocity vs. radial position at $z = 55$ cm under various superficial gas velocities. (c) Mean bubble velocity vs. radial position at $z = 95$ cm under various superficial gas velocities. (d) Mean bubble velocity vs. radial position at $z = 135$ cm under various superficial gas velocities. (e) Mean bubble velocity vs. radial position at $z = 175$ cm under various superficial gas velocities. (f) Mean bubble velocity vs. radial position at $z = 195$ cm under various superficial gas velocities. (g) Cross-sectionally averaged bubble velocity in the riser vs. axial position under various superficial gas velocities. (h) Mean downward bubble velocity in the downcomer vs. axial position under various superficial gas velocities.

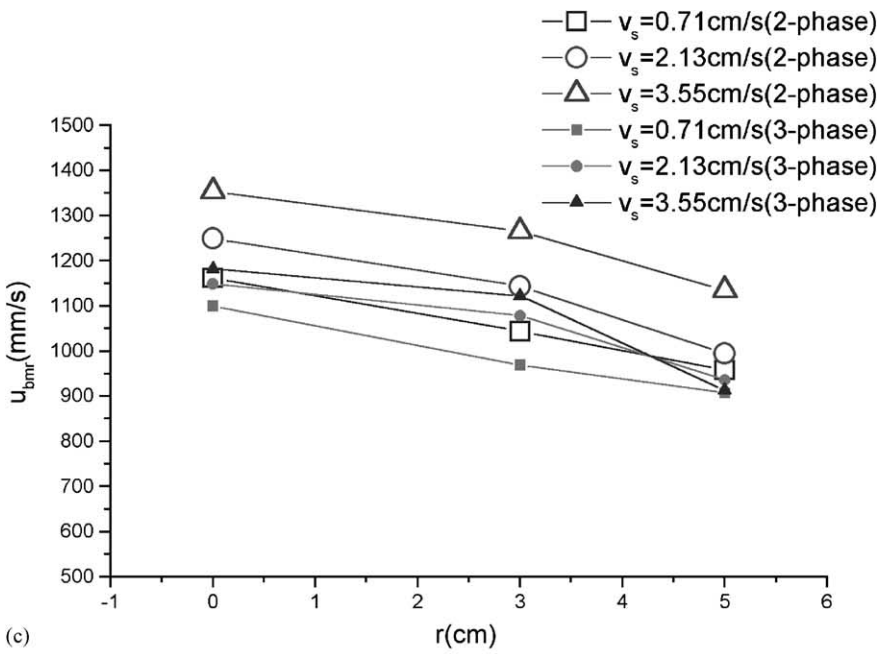

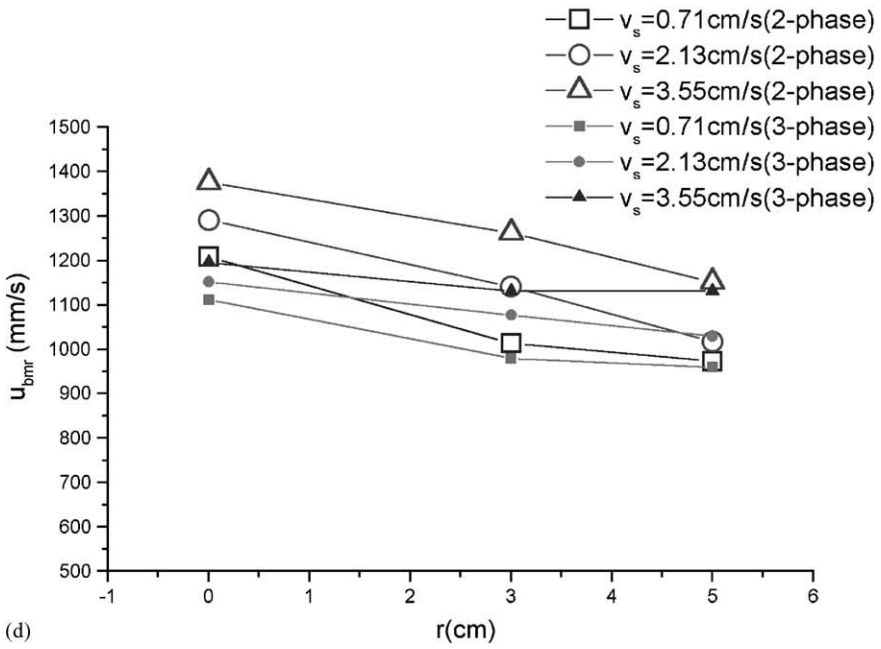

Fig. 14. (*Continued*).

The cross-sectionally averaged bubble size in the riser decreased with increasing axial distance at lower parts of the riser as shown in Fig. 13g. This was due to the fact that the gas emerging from the gas sparger are in the form of gas jets and the gas jet length is larger than the chord length of the resultant bubble. It is also seen in Fig. 13g that the bubble size increased with an increase in the axial distance. Similar phenomenon was reported by Rigby et al. [14]. They indicated that the bubble size distribution broadened and the mean bubble size increased with increasing axial distance from the distributor, and this increase in the bubble size with the axial distance was due to bubble coalescence. Since the mean bubble size in the two-phase system was larger than that in the three-phase system in this study, the extent of bubble coalescence in the two-phase system must be larger than that in the three-phase system. Fig. 13h shows that the mean bubble size in the downcomer varied irregularly with the axial distance. This was due to complex flow pattern in the downcomer.

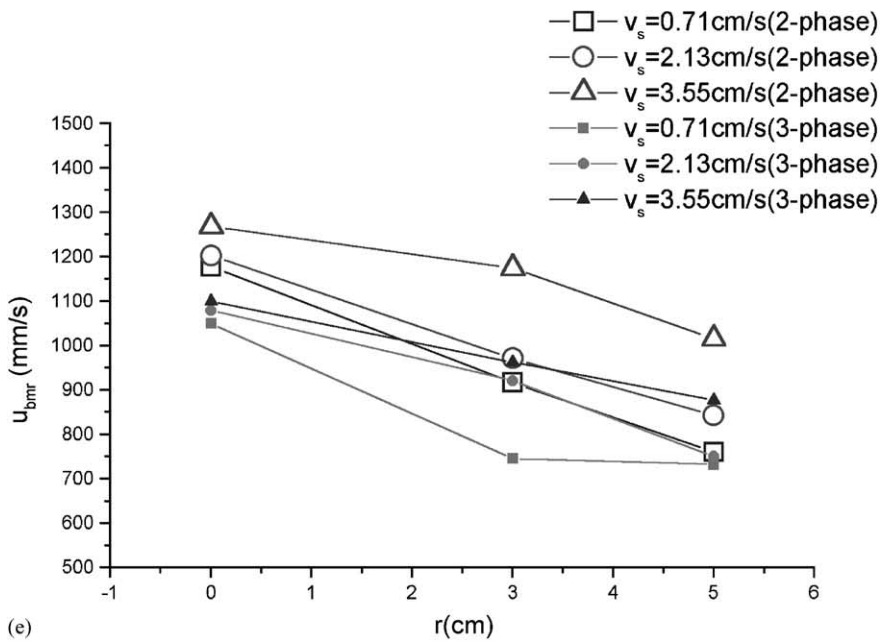

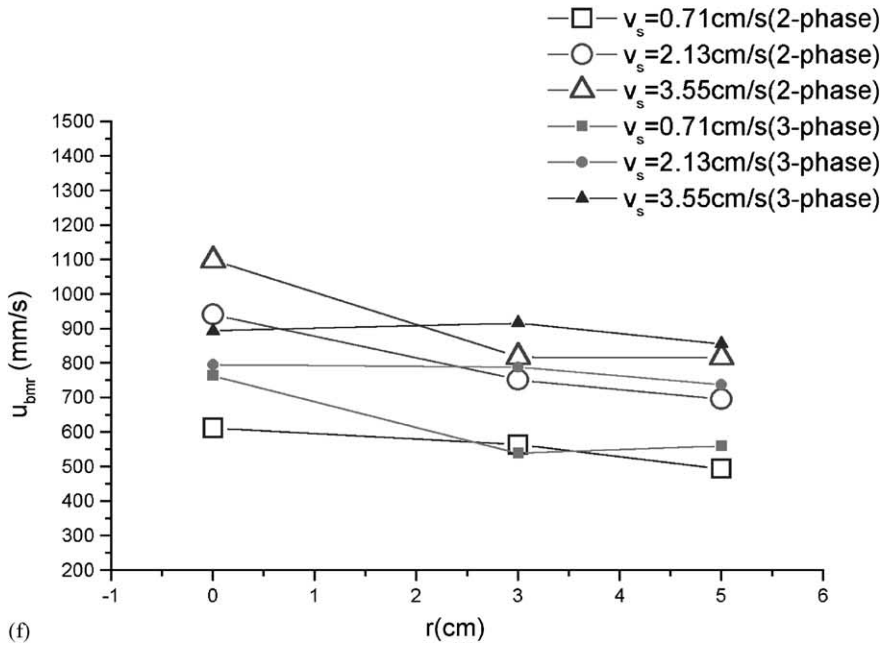

Fig. 14. (*Continued*).

3.2. Mean bubble velocity

Fig. 14a–f shows the radial profiles of the mean bubble velocity in the riser for the two-phase and three-phase systems as a function of the radial position under various superficial gas velocities and axial heights. It is seen in these figures that the mean bubble velocity of the three-phase system was lower than that of the two-phase system. The rise velocity of a bubble depends mainly on its size. Since the bubble size of the three-phase system was smaller than that of the two-phase system, the bubble velocity of the three-phase system was lower than that of the two-phase system. Also shown in Fig. 14a–f is that the radial variations of the bubble velocity for three-phase system were less than that for the two-phase system. Moreover, the mean bubble velocity increased with an increase in gas superficial velocity. This is due to the fact that a higher gas superficial velocity results in a larger bubble size and a higher liquid velocity [22]. As a consequence, the bubble velocity was higher for a higher gas velocity. Furthermore, the mean bubble

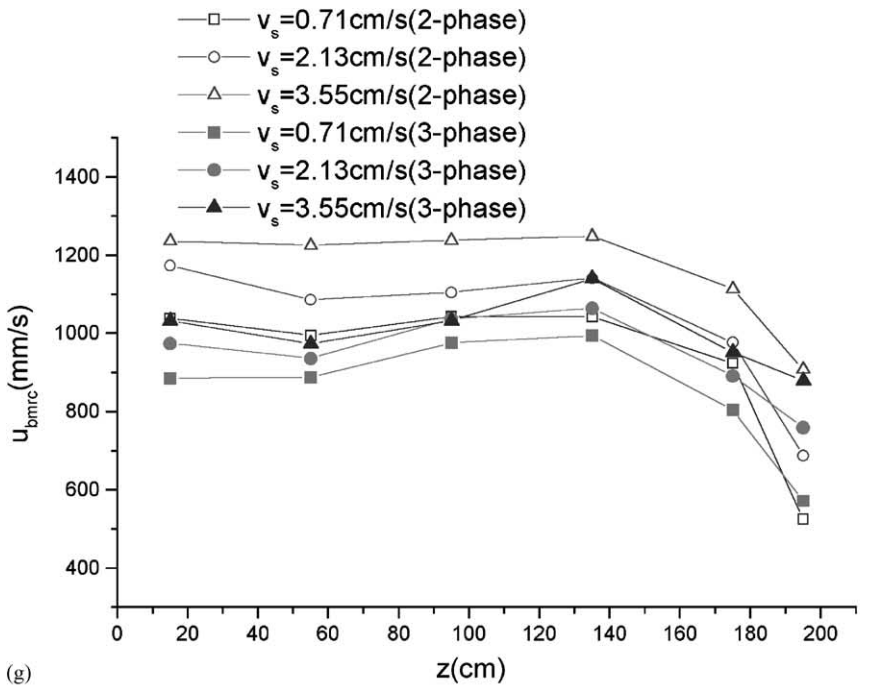

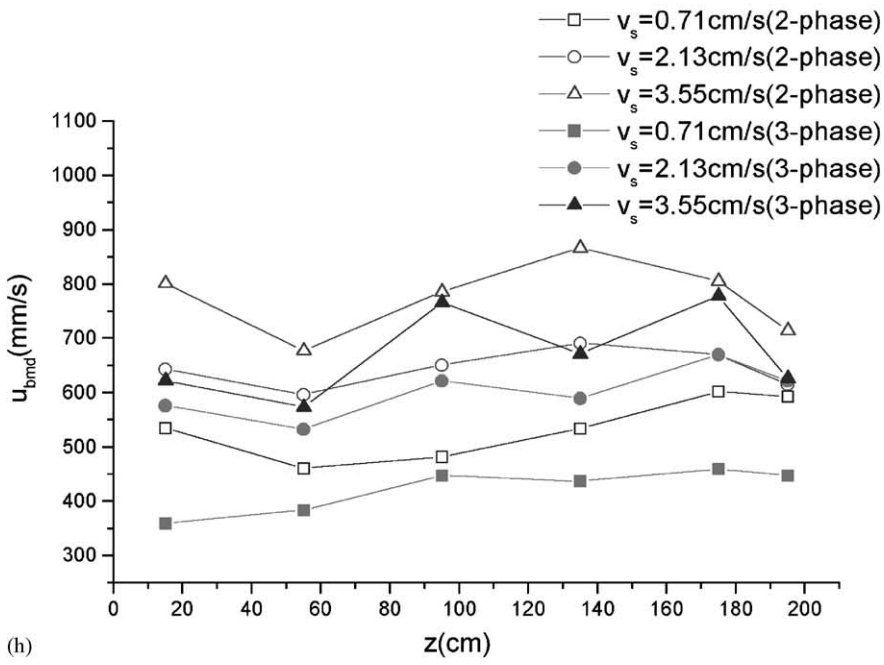

Fig. 14. (*Continued*).

velocity in the gas–liquid separator ($z = 195$ cm) was smaller than that near the top of the riser ($z = 175$ cm). This was due to the opposite flow directions of the gas and liquid in the gas–liquid separator (gas upward; liquid downward).

Fig. 14g shows the cross-sectionally averaged bubble velocity in the riser versus the axial position under various superficial gas velocities. The cross-sectionally averaged bubble velocity varied only slightly along the riser, and then decreased substantially near the top of the riser and in the gas–liquid separation region. This was similar to that shown in Fig. 14a–f for the mean bubble velocity. Fig. 14h shows the variations of the mean downward bubble velocity with the axial position. At the top of the riser, the downward liquid flow into the downcomer carried many small bubbles into the downcomer. Some of the small bubbles in the downcomer might coalesce to become larger bubbles and their net

downward velocity (downward velocity caused by the downward liquid flow—bubble rise velocity) decreased due to a higher rise velocity for a larger bubble. However, some of the larger bubbles might break up again and resulted in a larger downward bubble velocity. Therefore, there was no clear relationship between the bubble velocity in the downcomer and the axial position. It should be noted in Fig. 14h that near the bottom of the draft tube ($z = 15$ cm), the downward bubble velocity became larger. This might be due to liquid turn around at the bottom of the draft tube caused by the gas sparger.

3.3. Gas holdup

Fig. 15a–f shows the radial profiles of the gas holdup in the riser for the two-phase and three-phase systems as a

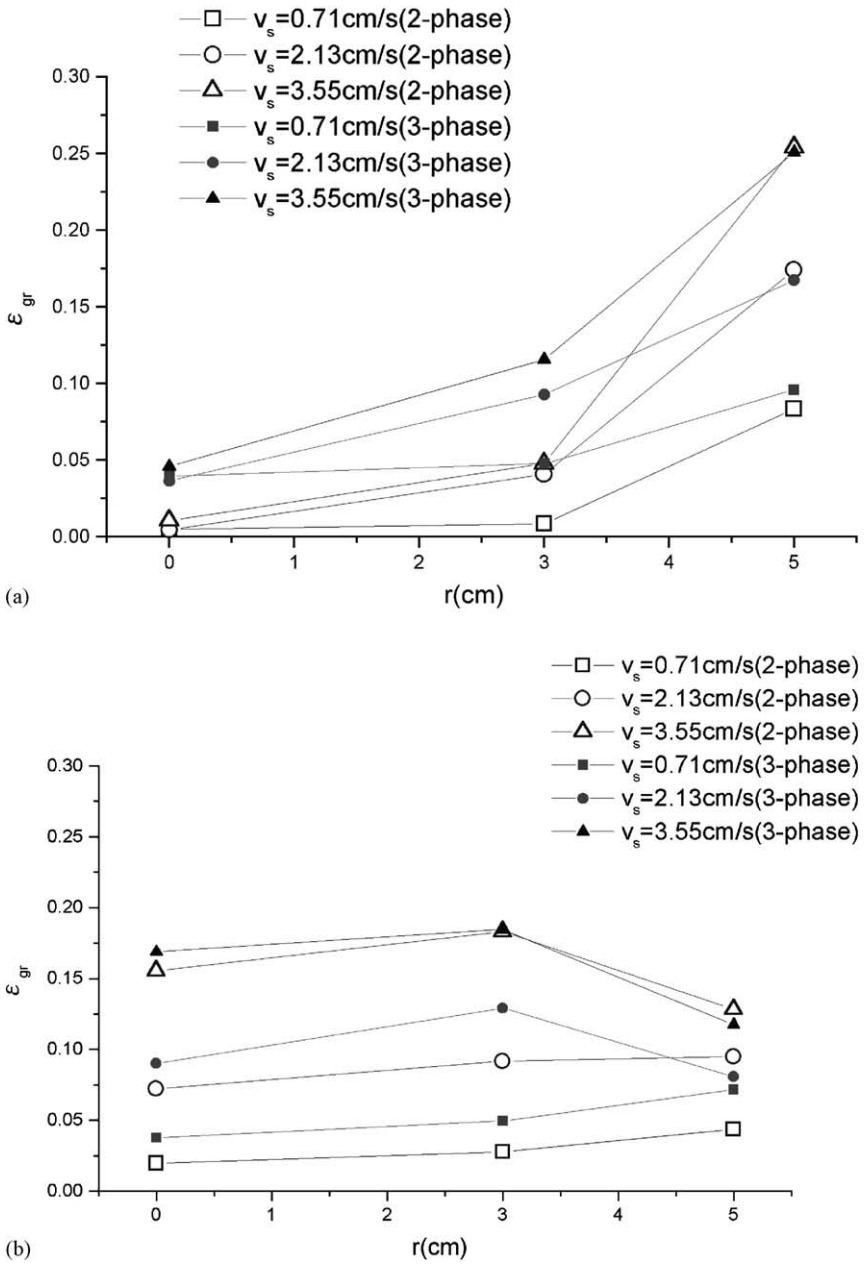

Fig. 15. (a) Gas holdup vs. radial position at $z = 15$ cm under various superficial gas velocities. (b) Gas holdup vs. radial position at $z = 55$ cm under various superficial gas velocities. (c) Gas holdup vs. radial position at $z = 95$ cm under various superficial gas velocities. (d) Gas holdup vs. radial position at $z = 135$ cm under various superficial gas velocities. (e) Gas holdup vs. radial position at $z = 175$ cm under various superficial gas velocities. (f) Gas holdup vs. radial position at $z = 195$ cm under various superficial gas velocities. (g) Cross-sectionally averaged gas holdup in the riser vs. axial position under various superficial gas velocities. (h) Gas holdup in the downcomer vs. axial position under various superficial gas velocities.

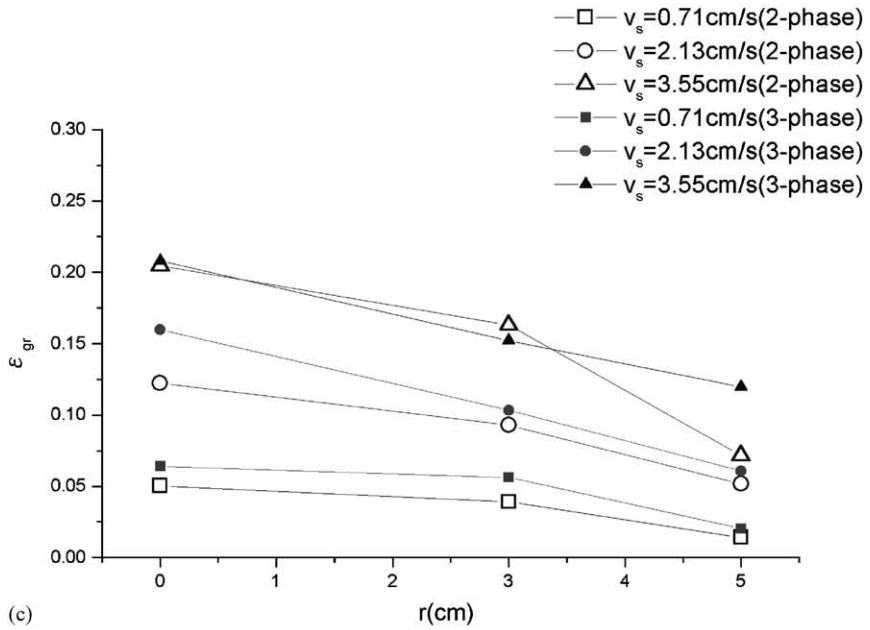

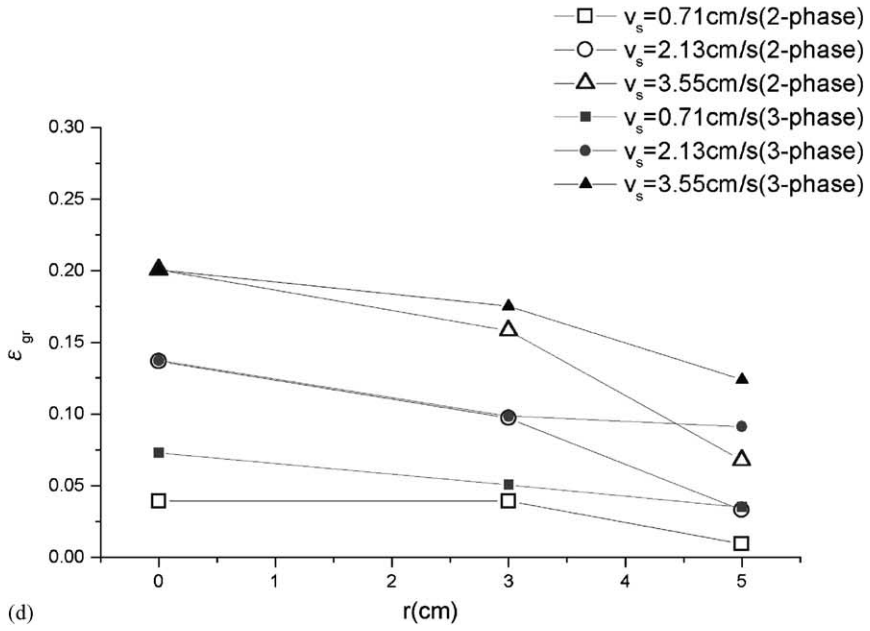

Fig. 15. (*Continued*).

function of radial position under various superficial gas velocities. As expected, the gas holdup increased with increasing gas velocity. At the riser bottom, the gas holdup was larger near the outer region of the riser owing to the location of the gas sparger (near the outer region of the riser). However, along the riser the gas holdup in the center region of the riser was higher than that in the outer region of the riser due to bubble aggregation in the center region of the riser. Moreover, the gas holdup of the three-phase system was larger than that of the two-phase system due to smaller bubbles for the three-phase system.

The cross-sectionally averaged gas holdup of the three-phase system was larger than that of two-phase system as shown in Fig. 15g. This was similar to that shown in Fig. 15a–f. In addition, the cross-sectionally averaged gas holdup was minimum and remained relatively unchanged in the middle part of the riser as shown in Fig. 15g. It is also seen in Fig. 15g that the cross-sectionally averaged gas holdup was the highest in the gas–liquid separator due to slower bubble velocities in this region. It should be noted in Figs. 14g and 15g that the gas holdup generally decreased with increasing bubble velocity. Fig. 15h shows

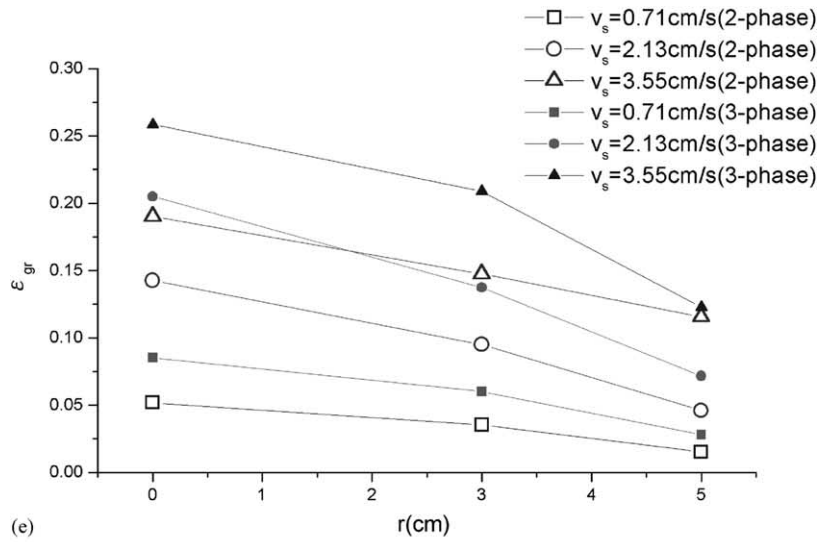

(e)

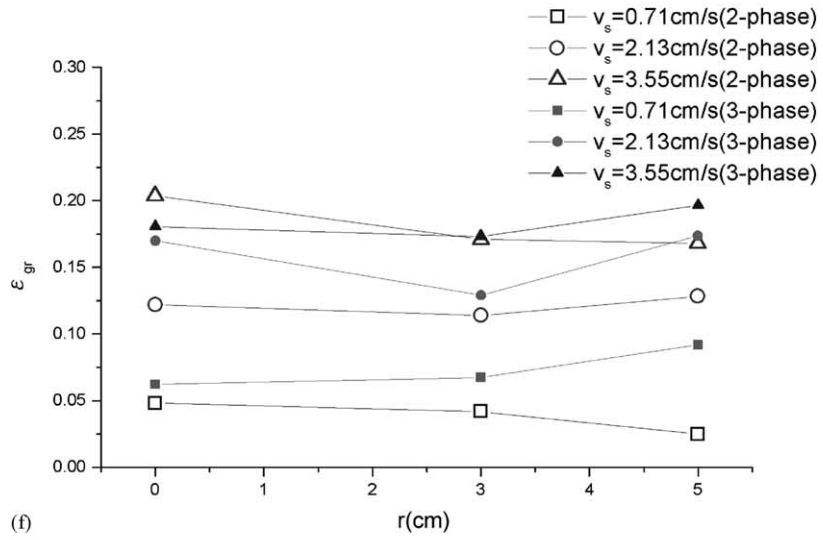

(f)

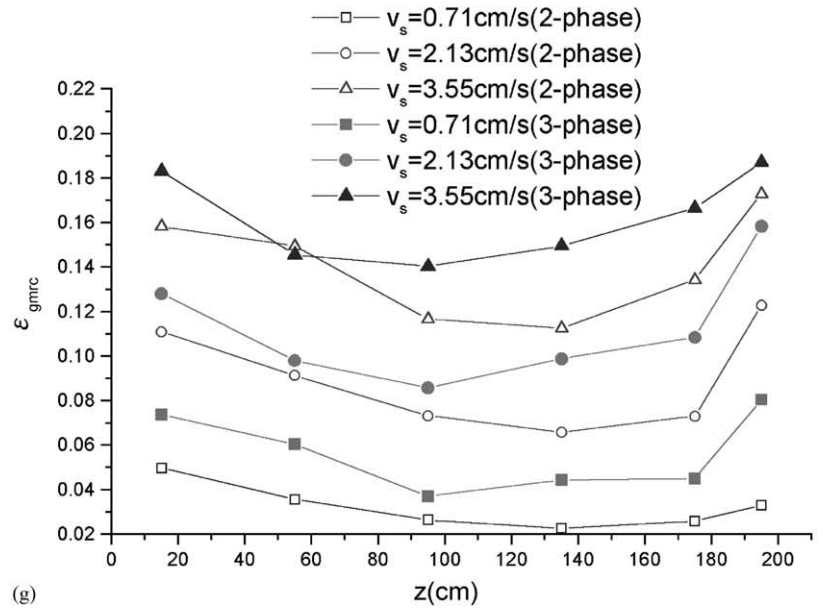

(g)

Fig. 15. (*Continued*).

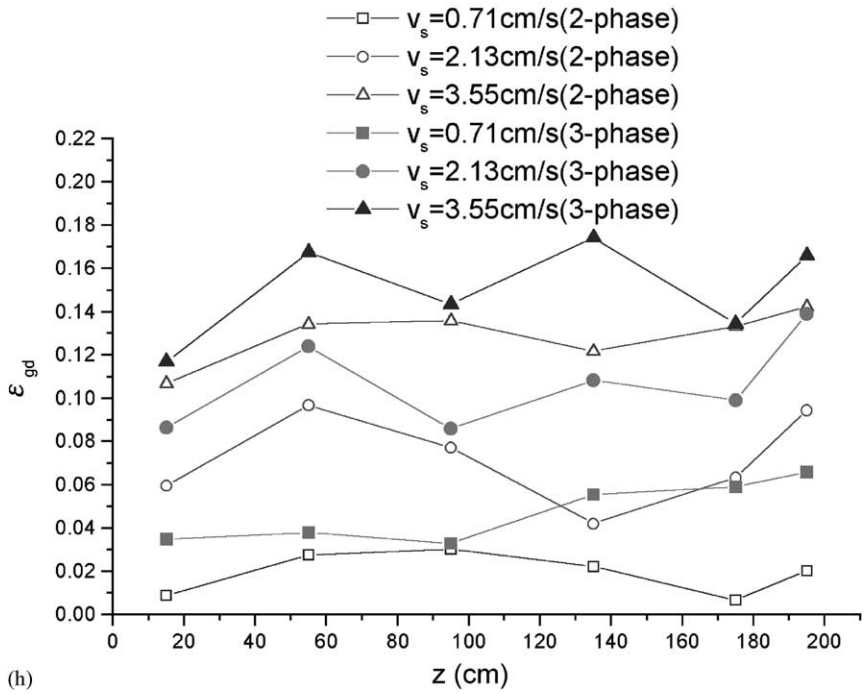

(h)

Fig. 15. (*Continued*).

the variations of the gas holdup in the downcomer with the axial position. Again, the gas holdup in the downcomer of the three-phase system was larger than that of two-phase system. This was due to the fact that the bubble velocity for the three-phase system is lower than that for the two-phase system.

4. Conclusions

This study indicated that larger bubbles tended to rise along the riser central axis and the variations of the bubble size, bubble velocity and gas holdup along the central axis were relatively small in the middle part of the riser. At the top of the riser and in the gas–liquid separator, the bubble size and the gas holdup became larger but the bubble velocity became slower. The variations of the gas-phase hydrodynamic properties in the downcomer with the axial position were irregular. This was because the flow patterns of the liquid and gas phases in the downcomer were far more complex than those in the riser. Therefore, no clear trend of the gas hydrodynamic behavior with the axial position in the downcomer was observed.

The results of this study also indicated that the gas holdup increased with decreasing bubble velocity. Furthermore, the bubble velocity and bubble size for the three-phase system were lower than those for the two-phase system, but the gas holdup for the three-phase system was higher than that for the two-phase system. This was due to bubble break up caused by the solid particles.

References

[1] M.Y. Chisti, Airlift Bioreactor, Elsevier, New York, 1989.
[2] A. Matsuura, L.S. Fan, AIChE J. 30 (1984) 894.
[3] L.S. Fan, K. Kitano, B.E. Kreischer, AIChE J. 33 (1987) 225.
[4] A. Yasunishi, M. Fukuma, K. Muroyama, J. Chem. Eng. Jpn. 19 (1986) 444.
[5] C. Bentifraouine, C. Xuereb, J.P. Riba, Bioprocess Eng. 20 (1999) 303.
[6] M. Utiger, F. Stuber, A.M. Duquenne, H. Delmas, C. Guy, Can. J. Chem. Eng. 77 (1999) 375.
[7] T. Miyahara, M. Hamaguchi, Y. Sukeda, T. Takahashi, Can. J. Chem. Eng. 64 (1986) 718.
[8] D.J. Gunn, H.H. Al-doori, Int. J. Multiphase Flow 11 (1985) 535.
[9] R. Buchholz, W. Zakrzewski, K. Schugerl, Int. Chem. Eng. 21 (1981) 180.
[10] C. Xuereb, J.P. Riba, Sens. Actu. A 46 (1995) 349.
[11] S.F. Moujaes, Can. J. Chem. Eng. (68) (1990) 504.
[12] N.N. Clark, W. Liu, R. Turton, Powd. Technol. 88 (1996) 179–188.
[13] K.I. Kikuchi, H. Takahashi, T. Koike, S. Chiba, J. Chem. Eng. Jpn. 32 (1999) 162.
[14] G.R. Rigby, G.P. Van Blockland, W.H. Park, C.E. Capes, Chem. Eng. Sci. 25 (1970) 1729.
[15] K. Ueyama, S. Morooka, K. Koide, H. Kaji, T. Miyauchi, IEC Process Des. Dev. 19 (1980) 592.
[16] W. Liu, N.N. Clark, Int. J. Multiphase Flow 21 (1995) 1073.
[17] T.Z. Harmathy, AIChE J. 6 (1960) 281.
[18] L.S. Fan, Gas–Liquid–Solid Fluidization Engineering, Butterworths, Boston, 1989.
[19] K.I. Kikuchi, H. Takahashi, F. Sugawara, S. Chiba, in: S. Uchida, S. Morooka (Eds.), Proceedings of the Seventh Asian Conference on Fluidized-bed and Three-phase Reactors, Shizuoka University, Japan, 2000, p. 551.
[20] K. Okada, Y. Nagata, Y. Akagi, J. Chem. Eng. Jpn. 29 (1996) 582.
[21] C. Wolff, F.U. Briegleb, J. Bader, K. Hector, H. Hammer, Chem. Eng. Technol. 13 (1990) 172.
[22] W.S. Tan, G.C. Dai, W. Ye, J.P. Shen, Chem. Eng. J. B 57 (1995) 31.